

# Prolonged orbital relaxation by locally modified phonon density of states for SiV<sup>-</sup> center in nanodiamonds

M. Klotz,<sup>1,\*</sup> K.G. Fehler,<sup>1,\*</sup> E. S. Steiger,<sup>1</sup> S. Häußler,<sup>1</sup> R. Waltrich,<sup>1</sup> P. Reddy,<sup>2</sup> L. F. Kulikova,<sup>3</sup> V. A. Davydov,<sup>3</sup> V. N. Agafonov,<sup>4</sup> M. W. Doherty,<sup>2</sup> and A. Kubanek<sup>1</sup>

<sup>1</sup>*Institute for Quantum Optics, Ulm University, 89081 Ulm, Germany*

<sup>2</sup>*Laser Physics Centre, Research School of Physics, Australian National University, Australian Capital Territory 2601, Australia*

<sup>3</sup>*L.F. Vereshchagin Institute for High Pressure Physics,*

*Russian Academy of Sciences, Troitsk, Moscow 142190, Russia*

<sup>4</sup>*GREMAN, UMR 7347 CNRS, INSA-CVL, Tours University, 37200 TOURS, France*

(Dated: January 1, 2022)

Coherent quantum systems are a key resource for emerging quantum technology. Solid-state spin systems are of particular importance for compact and scalable devices. However, interaction with the solid-state host degrades the coherence properties. The negatively-charged silicon vacancy center in diamond is such an example. While spectral properties are outstanding, with optical coherence protected by the defects symmetry, the spin coherence is susceptible to rapid orbital relaxation limiting the spin dephasing time. A prolongation of the orbital relaxation time is therefore of utmost urgency and has been tackled by operating at very low temperatures or by introducing large strain. However, both methods have significant drawbacks, the former requires use of dilution refrigerators and the latter affects intrinsic symmetries. Here, a novel method is presented to prolong the orbital relaxation with a locally modified phonon density of states in the relevant frequency range, by restricting the diamond host to below 100 nm. The method works at liquid Helium temperatures of few Kelvin and in the low-strain regime.

In recent years, solid-state quantum emitters have successfully been utilized for applications in quantum information science and sensing. Color centers in diamond, and in particular the negatively charged silicon vacancy center in diamond (SiV<sup>-</sup>), turned out to be a promising system to realize applications that rely on an efficient spin-photon interface and long-lived memories [1], for example in the context of quantum communication [2]. However, such sophisticated experiments require to suppress the strong influence from the host environment on the optical and spin coherence. Modifying the interaction with the environment enables to tailor the quantum properties towards the aforementioned applications. Here, the group-IV defect centers stand out by their inversion symmetric  $D_{3d}$  defect-structures which lead to protection of their optical transitions against charge-fluctuations from e.g. close-by surfaces, when integrated into nano-structures [3]. As a result, SiV<sup>-</sup> exhibit narrow inhomogeneous line distribution and excellent spectral stability [4]. Due to its relatively small orbital extension as compared to other group IV defects, SiV<sup>-</sup> is highly susceptible to strain introduced by electron-phonon interactions with the environment [5]. On the one hand, this opens up the possibility to use the SiV<sup>-</sup> as a coherent spin-phonon interface for potential transduction between different quantum systems [6]. On the other hand, the spin coherence time is limited due to fast dephasing processes related to orbital transitions in the groundstate [7]. For temperatures below 25 K, the orbital relaxation rate is dominated by a single acoustic phonon process, resonant to the ground state splitting (GS splitting) of

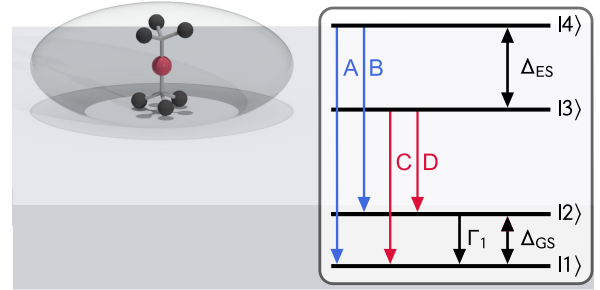


FIG. 1. Schematic of a geometrically confined SiV<sup>-</sup> within a ND placed on a diamond substrate. The defects level structure is also depicted with its zero-phonon-line transitions A, B, C and D. The GS splitting  $\Delta_{GS}$  is a result from spin-orbit as well as mechanical interaction with the environment, which leads to an orbital relaxation from  $|2\rangle \rightarrow |1\rangle$  with rate  $\Gamma_1$ , where e.g.  $|2\rangle = |e_{g-} \uparrow\rangle$  and  $|1\rangle = |e_{g+} \uparrow\rangle$  in a strain-free environment.

$\Delta_{GS}/2\pi \approx 46$  GHz as a result of spin-orbit (SO) interaction [8]. Therefore, in high-purity, low-strain bulk diamond the orbital relaxation time ( $T_1$ ) is limited to between 10 ns and 40 ns for temperatures from 25 K to 7 K. Hence, decreasing the ground state orbital relaxation rate ( $\Gamma_1$ ) is crucial for future applications that rely on a long spin coherence time ( $T_2$ ). As a result, one ambition is to increase  $T_1 = \Gamma_1^{-1}$  so that the spin dephasing time  $T_2^*$  is no longer limited by orbital relaxation but rather by intrinsic, material related noise sources, such as dipolar coupling to the nuclear spin bath or g-factor fluctuations.

In general, there are two possibilities to potentially influence  $\Gamma_1$ . First, decreasing the temperature reduces

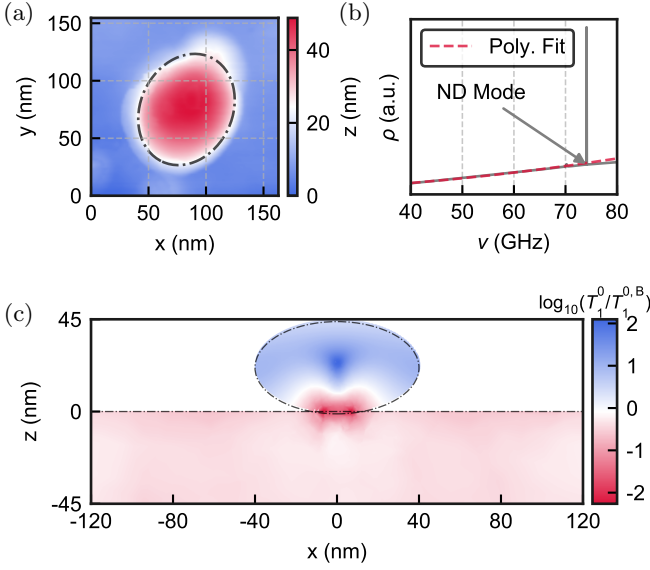


FIG. 2. (a) AFM scan of a ND revealing characteristic sizes of  $(r_x, r_y, r_z) = (40, 50, 22.5)$  nm, setting an upper size limit for all consecutively measured ND samples. (b) Density of states (DOS)  $\rho$  as a function of frequency  $\nu$  for the ND coupled to bulk with a penetration depth of  $d = 0.01r_z$ . A polynomial fit shows a scaling of  $\rho \propto \nu^{1.91}$  for the composite system. (c) FEM simulation of the relative local increase in orbital relaxation times compared to bulk,  $T_1^0/T_1^{0,B}$ .

thermal occupation of phonon modes at the relevant frequencies  $\Delta_{GS}$  [1]. Experiments have been performed at temperatures of 100 mK yielding  $T_2 = 13 \mu\text{s}$ , where  $k_B T \ll \hbar \Delta_{GS}$ . Already at 2-4 K the spin dephasing time of about  $T_2^* = 100$  ns is significantly shortened [1, 9]. Second, changing the geometry or applying an external load alters the  $\text{SiV}^-$  strain environment and hence locally modifies the spectral coupling density. Imposing an external force has been done by means of a nano-electro-mechanical system, which resulted in prolonged  $T_2^*$  of  $0.25 \mu\text{s}$  for a GS splitting of 467 GHz [10].

This work presents an orbital lifetime extension of  $\text{SiV}^-$ , that are incorporated into a geometrically confined host, namely a nanodiamond (ND), as illustrated in Fig. 1. In order to achieve cold temperatures at the position of the  $\text{SiV}^-$  the ND is in direct thermal contact with a cooled base substrate which inevitably leads to a phononic coupling between the ND and the base substrate. Numerical simulations of a ND coupled to a diamond base substrate give detailed insights into the  $\text{SiV}^-$  strain response as well as phononic coupling to the substrate. The results are compared with measurements of 14 NDs with varying GS splitting and temperatures.

*Model* – The groundstate manifold  $\text{SiV}^-$  Hamiltonian considered here is given by ( $\hbar = 1$ )

$$\begin{aligned} H_{\text{SiV}} = & \frac{\lambda_{\text{SO}}}{2} \sigma_{y,o} \otimes \sigma_{z,s} \\ & + \chi_{\text{E}_{\text{gx}}} \epsilon_{\text{E}_{\text{gx}}} \sigma_{z,o} \otimes \mathbb{1}_s + \chi_{\text{E}_{\text{gy}}} \epsilon_{\text{E}_{\text{gy}}} \sigma_{x,o} \otimes \mathbb{1}_s \end{aligned} \quad (1)$$

where  $\sigma_{x,o} = |e_x\rangle \langle e_y| + |e_x\rangle \langle e_y|$ ,  $\sigma_{y,o} = -i|e_x\rangle \langle e_y| + i|e_y\rangle \langle e_x|$  and  $\sigma_{z,o} = |e_x\rangle \langle e_x| - |e_y\rangle \langle e_y|$  are orbital and  $\sigma_{z,s} = |\uparrow\rangle \langle \uparrow| - |\downarrow\rangle \langle \downarrow|$  are spin operators.  $\lambda_{\text{SO}} = 46$  GHz describes the spin-orbit interaction strength, which lifts the degeneracy by mixing orbital and spin degrees of freedom, to create  $|e_{g\pm}\rangle |\uparrow(\downarrow)\rangle = 1/\sqrt{2}(|e_x\rangle \pm i|e_y\rangle) |\uparrow(\downarrow)\rangle$  [11]. The strain energies  $\chi_r \epsilon_r$  are symmetry adapted linear combinations of strain field components  $\epsilon_{ij}$  and strain susceptibilities  $\alpha, \beta$  corresponding to irreducible representations  $r$  of  $D_{3d}$

$$\chi_{\text{E}_{\text{gx}}} \epsilon_{\text{E}_{\text{gx}}} = \alpha(\epsilon_{xx} - \epsilon_{yy}) + \beta \epsilon_{zx} \quad (2)$$

$$\chi_{\text{E}_{\text{gy}}} \epsilon_{\text{E}_{\text{gy}}} = -2\alpha \epsilon_{xy} + \beta \epsilon_{yz}, \quad (3)$$

where  $\epsilon_{ij}$  are expressed within the defect internal basis [12]. Diagonal terms involving  $\epsilon_{A_{1g}}$  are neglected in Eq. (1), as they only shift the total energy. As a consequence of the mechanical interaction, the pure spin-orbit states  $|e_{g+}\uparrow\rangle, |e_{g-}\downarrow\rangle$  and  $|e_{g+}\downarrow\rangle, |e_{g-}\uparrow\rangle$  with an energy splitting of  $\Delta_{GS}/2\pi = \lambda_{\text{SO}}$  will shift in relative energies and also undergo relaxations with rate  $\Gamma_1$ , see Fig. 1. The strain-dependent transition rates from the excited to the ground state are calculated in the above basis by Fermi's golden rule ( $T \rightarrow 0$ )

$$\begin{aligned} \Gamma_1^0 = & 2\pi \sum_n \left( |\chi_{\text{E}_{\text{gx}}} \epsilon_{\text{E}_{\text{gx}},n}|^2 + |\chi_{\text{E}_{\text{gy}}} \epsilon_{\text{E}_{\text{gy}},n}|^2 \right) \\ & \times \delta(\omega_n - \Delta_{GS}). \end{aligned} \quad (4)$$

Here  $n$  labels the various coupled system eigenfrequencies.

The potential local increase in  $T_1^0$  compared to bulk  $T_1^{0,B}$  is estimated by utilizing 3D-FEM to solve for the mechanical eigenfrequencies of a ND coupled to a diamond substrate. The material properties are assumed to be isotropic with mass density  $\rho = 3515 \text{ kg m}^{-3}$ , Young's modulus  $E = 1050 \text{ GPa}$  and Poisson ratio  $\nu = 0.2$  [12, 13]. Differing material parameters are discussed in the supplementary information.

The NDs within our size range of 30-100 nm exhibit a pronounced cubo-octahedral geometry. The numerically simulated ND is approximated with a more symmetrical ellipsoidal geometry, whose semi-axis are extracted from an atomic force microscope (AFM) scan with  $(r_x, r_y, r_z) = (40, 50, 22.5)$  nm, see Fig. 2(a). In addition, slightly immersing the ND along  $z$  into the substrate with a penetration depth  $d = \xi r_z$  creates a contact area, where phonons can be exchanged with the bulk reservoir and hence introduce a coupling rate. Fig. 2(b) shows the simulated spectral density of states (DOS)

$\rho(\nu)$  for the aforementioned ND coupled to bulk with  $\xi = 10^{-2}$ , which reveals a quasi localized ND mode around 75 GHz. Moreover, a polynomial fit (red dashed line in Fig. 2(b)) shows that the DOS approximately scales with  $\rho(\nu) \propto \nu^{1.91}$  rather than quadratically which is to be expected for a pure bulk-like system in the Debye limit. This indicates contributions from bound surface modes [10, 14]. For details on the DOS evaluation, see supplementary information.

Using the strain susceptibilities  $\alpha = 1.3$  PHz/Strain,  $\beta = 1.7$  PHz/Strain in Eq. (2) & (3), as well as the simulated strain fields  $\epsilon_{ij,n}(\vec{r})$  of the coupled system, where the SiV<sup>-</sup> high-symmetry axis is assumed along  $z$ , Eq. (4) is evaluated at each position in the  $xz$ -plane [5]. For this the delta-distributions  $\delta_n = \delta(\omega_n - \Delta_{GS})$  are approximated with Lorentzians and the correspondingly simulated eigenfrequencies  $\omega_n$  as well as decay rates  $\gamma_n = \omega_n/Q_n$  are used, where  $Q_n$  is the respective mechanical quality factor. Fig. 2(c) shows the orbital lifetime ratio  $T_1^0/T_1^{0,B}$ , where  $T_1^{0,B} \approx 209$  ns is obtained by averaging  $T_1^0$  over the bulk which is in good agreement with the analytical  $T_1^{0,B} \approx 233$  ns. Note that Fig. 2(c) only shows a close-up of the ND in the  $xz$ -plane. Further details on the whole simulation are presented in the supplementary information. The already discussed presence of surface acoustic waves, bound to the diamond interface, also increases strain and hence leads to a reduction in  $T_1^0$  [6]. At the contact area, where strain fields are largest, the relaxation rate is maximal with two orders of magnitude smaller decay time than the average  $T_1^{0,B}$ . However, the current configuration reaches a maximum of  $T_{1,\max}^0/T_1^{0,B} \approx 120$  at the center of the ND. Even in the upper half of the ND, relaxation time is enhanced by approximately an order of magnitude. As a rough estimate,  $T_{1,\max}^0$  would extend the orbital lifetime at cryogenic temperatures of  $T = 5$  K to  $T_{1,\max} = \coth(\hbar\Delta_{GS}/2k_B T)T_{1,\max}^0 \approx 5$   $\mu$ s.

*Measurements* –  $T_1$  is measured for 14 SiV<sup>-</sup> in NDs at temperatures ranging from 4.6 K up to 9.5 K. The NDs are coated onto a diamond substrate, selected for high thermal conductivity. Using an AFM, the average size of the NDs is determined to be 30 nm. The temperature of each SiV<sup>-</sup> is evaluated by dividing the sum of normalized counts in transition C and D ( $C_{C+D}$ ) by the respective counts in A and B ( $C_{A+B}$ ), which reflects the relative population in the lower and upper excited state, see Fig. 3(a). Assuming a Boltzmann distribution for the latter, the temperature can be calculated with

$$\frac{C_{C+D}}{C_{A+B}} = \exp\left(-\frac{\hbar\Delta_{ES}}{k_B T}\right). \quad (5)$$

The excited state splitting (ES splitting) is determined from the spectrum of an off-resonantly excited SiV<sup>-</sup>. Fig. 3(a) shows an example ND spectrum.

Resonant excitation of transition C is achieved with

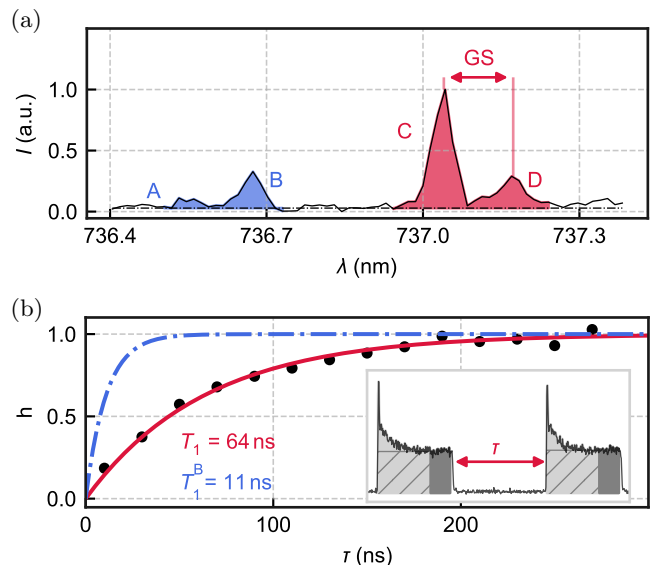


FIG. 3. (a) Photo-luminescence intensity  $I$  as a function of wavelength  $\lambda$  revealing the four-line structure of a SiV<sup>-</sup> in an ND with a GS splitting of 73 GHz. The temperature of the SiV<sup>-</sup> is determined using Boltzmann distributed populations and summing over transition A+B and C+D. (b) Peak heights  $h$ , determined from the fluorescence of a resonant pulse sequence, as a function of inter-pulse delay  $\tau$ . The solid red line shows a numerical fit revealing  $T_1 = 64$  ns, whereas the dash-dotted blue line depicts a correspondingly theoretical bulk recovery with  $T_1^B = 11$  ns as a comparison. The inset illustrates the extraction of the peak heights with the extrapolation of the stationary count rate (horizontal solid line) by the last 50 ns countrace (dark grey area).

a tunable single-frequency Ti:sapphire laser and fluorescence from the phonon-sideband is detected using a 750 nm longpass filter in front a single-photon counter to block the laser. Additionally, a weak 532 nm laser is utilized to stabilize the emission.  $T_1$  is measured with a tailored pulse-sequence, consisting of several 200 ns-long pulses with an increasing inter-pulse delay  $\tau$  [15]. The peak heights are extracted by summing up all counts within each pulse and subtracting the stationary ones. The latter is estimated by extrapolating a stationary count rate using the last 50 ns and multiplying it by the corresponding pulse length, as depicted in the inset of Fig. 3(b). The peak heights  $h$  are then fitted with

$$h(\tau) \propto 1 - \exp\left(-\frac{\tau}{T_1}\right), \quad (6)$$

revealing a  $T_1$  of  $(64 \pm 3)$  ns for the SiV<sup>-</sup> measured in Fig. 3(b).

To compare our measured values for  $T_1$  at different temperatures  $T$  and GS splitting  $\Delta_{GS}$  to the correspond-

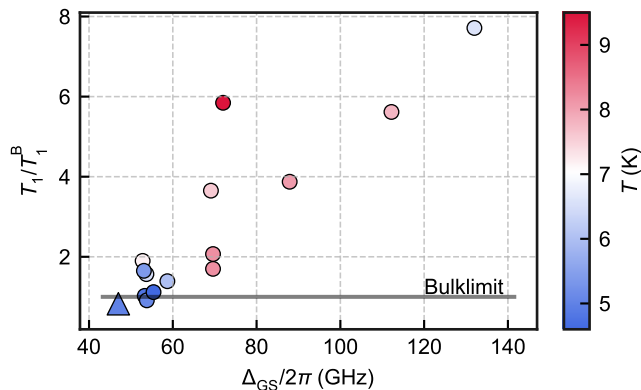


FIG. 4. Orbital lifetime extension through comparison of measured  $T_1$  and analytical bulk-limit  $T_1^B$  for different GS splitting  $\Delta_{GS}$  and temperatures  $T$ . The triangularly shaped marker represents a measured  $T_1 = 38$  ns in bulk from reference [8].

ing bulk time  $T_1^B$ , an analytical expression

$$(T_1^B)^{-1} = \frac{\hbar(\alpha^2 + (\beta/2)^2)}{\pi\rho} \left( \frac{1}{5v_t^5} + \frac{2}{15v_l^5} \right) \left( \frac{\Delta_{GS}}{2\pi} \right)^3 \times \coth \left( \frac{\hbar\Delta_{GS}}{2k_B T} \right), \quad (7)$$

with

$$v_t = \sqrt{\frac{E}{\rho} \frac{1}{2(1+\nu)}} \quad v_l = \sqrt{\frac{E}{\rho} \frac{1-\nu}{(1+\nu)(1-2\nu)}}$$

is used. Eq. (7) can be derived from Eq. (4) using a long-wavelength approximation [14, 16]. For the  $T_1$  measurement shown in Fig. 3(b), the corresponding ND temperature of  $T = 9.5$  K and GS splitting  $\Delta_{GS}/2\pi = 72$  GHz together with Eq. (7) are used to calculate a bulk orbital relaxation time of  $T_1^B = 11$  ns. Hence, an increase by a factor of  $64 \text{ ns}/11 \text{ ns} \approx 6$  for this ND is achieved. The procedure is repeated for all other 13 NDs and the ratio  $T_1/T_1^B$  is depicted in Fig. 4 as a function of GS splitting. The color of each dot shows the temperature of the respective SiV<sup>-</sup>. For a GS splitting of 132 GHz a prolongation of the orbital lifetime of up to 8 can be observed. The triangularly shaped marker represents a measured  $T_1$  in bulk which was conducted under similar experimental conditions [8]. The above calculated  $T_1^B$  is a conservative estimation of the upper limit reachable in bulk-diamond in the presence of resonant, single-phonon dominated orbital relaxation. To our knowledge experimentally measured  $T_1^B$  in the low-strain regime do not reach the theoretical limit [17, 18].

*Discussion* – The results in Fig. 4 suggest an inverse correlation between  $T_1/T_1^B$  and ND size. On the one hand, reducing the size shifts the NDs mechanical eigenfrequencies to higher energies [16], which also enhances

the respective modes strain field [8, 12]. As a result a SiV<sup>-</sup> can couple to these fields, which increases its GS splitting. Consequential, thermally excited phonons from the surrounding ND or bulk are exponentially less likely populated, thus reducing  $\Gamma_1$ . On the other hand, smaller SiV<sup>-</sup> host geometries exhibit reduced contact areas between the ND and the substrate which then suppress coupling to the bulk phonon bath, hence also reducing  $\Gamma_1$ . The supplementary information provides further simulations with a different geometry compared to Fig. 2, various contact areas and ground-state splittings. Geometrical decoupling becomes apparent, when looking at NDs with  $\Delta_{GS}/2\pi \approx 70$  GHz in Fig. 4. The similar GS splittings indicate correspondingly comparable ND geometries. However, the one with a maximal temperature of  $T = 9.5$  K, exhibits an orbital lifetime ratio of  $T_1/T_1^B \approx 6$ , which is largest for those NDs under consideration. This might reveal a preferential orientation of the ND, whose contact area with the substrate is smallest and thus also isolated best. As a result the phonon exchange with the substrate is reduced which reduces  $\Gamma_1$  and increases temperature, too. The discrepancy between simulated orbital lifetime ratios and the ones which are determined from measurements is attributed to an unfavorable interplay of different mechanisms, leading to non-trivial coupling rates to the bulk. These broaden the ND resonances and thus bring their local phononic spectral densities closer to the one of bulk which limit the maximally achievable  $T_1/T_1^B$ . Firstly, although the NDs sizes are measured to be smaller than the simulated one, a contact area largely exceeding the one used in the simulation strongly enhances phonon exchange with the bulk. Secondly, the mechanical impedances of the ND and the diamond base substrate are similar, allowing for a high phonon transmission, which also increases coupling to the substrate.

*Outlook* – The experimental results presented in this work show that the SiV<sup>-</sup> orbital lifetime is extended by a factor of 8 when incorporated into a small, tailored diamond host as compared to a SiV<sup>-</sup> in bulk-diamond. In order to suppress the orbital relaxation further, nanomanipulation techniques utilizing an AFM can be used to rotate the NDs, thereby lowering the area of contact which leads to a more optimal isolation [15, 19]. In addition, using a substrate material which is engineered to suppress phonons in the relevant spectral range also reduces the impedance matching between the former and the ND, which yields a better isolated host. For this purpose, a phononic crystal with a suitable bandgap could be used [13]. Ultimately, the concepts could be applied to experiments with levitated NDs [20–22].

The SiV<sup>-</sup> spin dephasing time  $T_2^*$  is mainly limited by orbital relaxation processes involving single phonons at temperatures around 5 K [17], with  $T_2^* \approx 2T_1$  [18, 23]. Hence, extending  $T_1$  to the predicted 5  $\mu$ s opens up the possibility to coherently control the SiV<sup>-</sup> spin without

relying on a dilution refrigerator, since mechanical decoupling from thermal phonons was shown for temperatures below 500 mK [1]. Thus in this regime,  $T_2^*$  is no longer limited by single phonon processes.

Moreover, due to the NDs integration capability into photonic structures, passive photonic and phononic properties could be merged and leveraged to achieve coherent spin-photon control [24].

## ACKNOWLEDGMENTS

The project was funded by the Deutsche Forschungsgemeinschaft (DFG, German Research Foundation) in project 398628099, the Baden-Württemberg Stiftung in project Internationale Spitzenforschung and IQst. MWD acknowledges support from the Australian Research Council (DE170100169). Experiments performed for this work were operated using the Qudi software suite [25].

\* These authors contributed equally.

- [1] D. D. Sukachev, A. Sipahigil, C. T. Nguyen, M. K. Bhaskar, R. E. Evans, F. Jelezko, and M. D. Lukin, Silicon-Vacancy Spin Qubit in Diamond: A Quantum Memory Exceeding 10 ms with Single-Shot State Readout, *Phys. Rev. Lett.* **119**, 223602 (2017).
- [2] M. K. Bhaskar, R. Riedinger, B. Machielse, D. S. Levonian, C. T. Nguyen, E. N. Knall, H. Park, D. Englund, M. Lončar, D. D. Sukachev, and M. D. Lukin, Experimental demonstration of memory-enhanced quantum communication, *Nature* **580**, 60 (2020).
- [3] J. L. Zhang, S. Sun, M. J. Burek, C. Dory, Y.-K. Tzeng, K. A. Fischer, Y. Kelaita, K. G. Lagoudakis, M. Radulaski, Z.-X. Shen, N. A. Melosh, S. Chu, M. Lončar, and J. Vučković, Strongly Cavity-Enhanced Spontaneous Emission from Silicon-Vacancy Centers in Diamond, *Nano Lett.* **18**, 1360 (2018).
- [4] J. Lang, S. Häußler, J. Fuhrmann, R. Waltrich, S. Laddha, J. Scharpf, A. Kubanek, B. Naydenov, and F. Jelezko, Long optical coherence times of shallow-implanted, negatively charged silicon vacancy centers in diamond, *Appl. Phys. Lett.* **116**, 064001 (2020).
- [5] S. Meesala, Y.-I. Sohn, B. Pingault, L. Shao, H. A. Atikian, J. Holzgrafe, M. Gündoğan, C. Stavarakas, A. Sipahigil, C. Chia, R. Evans, M. J. Burek, M. Zhang, L. Wu, J. L. Pacheco, J. Abraham, E. Bielejec, M. D. Lukin, M. Atatüre, and M. Lončar, Strain engineering of the silicon-vacancy center in diamond, *Phys. Rev. B* **97**, 205444 (2018).
- [6] S. Maity, L. Shao, S. Bogdanović, S. Meesala, Y.-I. Sohn, N. Sinclair, B. Pingault, M. Chalupnik, C. Chia, L. Zheng, K. Lai, and M. Lončar, Coherent acoustic control of a single silicon vacancy spin in diamond, *Nat Commun* **11**, 193 (2020).
- [7] B. Pingault, D.-D. Jarausch, C. Hepp, L. Klintberg, J. N. Becker, M. Markham, C. Becher, and M. Atatüre, Coherent control of the silicon-vacancy spin in diamond, *Nat Commun* **8**, 15579 (2017).
- [8] K. D. Jahnke, A. Sipahigil, J. M. Binder, M. W. Doherty, M. Metsch, L. J. Rogers, N. B. Manson, M. D. Lukin, and F. Jelezko, Electron-phonon processes of the silicon-vacancy centre in diamond, *New J. Phys.* **17**, 043011 (2015).
- [9] M. H. Metsch, K. Senkalla, B. Tratzmiller, J. Scheuer, M. Kern, J. Achard, A. Tallaire, M. B. Plenio, P. Siyushev, and F. Jelezko, Initialization and Readout of Nuclear Spins via a Negatively Charged Silicon-Vacancy Center in Diamond, *Phys. Rev. Lett.* **122**, 190503 (2019).
- [10] Y.-I. Sohn, S. Meesala, B. Pingault, H. A. Atikian, J. Holzgrafe, M. Gündoğan, C. Stavarakas, M. J. Stanley, A. Sipahigil, J. Choi, M. Zhang, J. L. Pacheco, J. Abraham, E. Bielejec, M. D. Lukin, M. Atatüre, and M. Lončar, Controlling the coherence of a diamond spin qubit through its strain environment, *Nat Commun* **9**, 2012 (2018).
- [11] C. Hepp, T. Müller, V. Waselowski, J. N. Becker, B. Pingault, H. Sternschulte, D. Steinmüller-Nethl, A. Gali, J. R. Maze, M. Atatüre, and C. Becher, Electronic Structure of the Silicon Vacancy Color Center in Diamond, *Phys. Rev. Lett.* **112**, 036405 (2014).
- [12] M.-A. Lemonde, S. Meesala, A. Sipahigil, M. J. A. Schuetz, M. D. Lukin, M. Loncar, and P. Rabl, Phonon Networks with Silicon-Vacancy Centers in Diamond Waveguides, *Phys. Rev. Lett.* **120**, 213603 (2018).
- [13] I. Lekavicius, T. Oo, and H. Wang, Diamond Lamb wave spin-mechanical resonators with optically coherent nitrogen vacancy centers, *Journal of Applied Physics* **126**, 214301 (2019).
- [14] K. V. Kepesidis, M.-A. Lemonde, A. Norambuena, J. R. Maze, and P. Rabl, Cooling phonons with phonons: Acoustic reservoir engineering with silicon-vacancy centers in diamond, *Phys. Rev. B* **94**, 214115 (2016).
- [15] S. Häußler, L. Hartung, K. G. Fehler, L. Antoniuk, L. F. Kulikova, V. A. Davydov, V. N. Agafonov, F. Jelezko, and A. Kubanek, Preparing single SiV<sup>-</sup> center in nanodiamonds for external, optical coupling with access to all degrees of freedom, *New J. Phys.* **21**, 103047 (2019).
- [16] A. Albrecht, A. Retzker, F. Jelezko, and M. B. Plenio, Coupling of nitrogen vacancy centres in nanodiamonds by means of phonons, *New J. Phys.* **15**, 083014 (2013).
- [17] L. J. Rogers, K. D. Jahnke, M. H. Metsch, A. Sipahigil, J. M. Binder, T. Teraji, H. Sumiya, J. Isoya, M. D. Lukin, P. Hemmer, and F. Jelezko, All-Optical Initialization, Readout, and Coherent Preparation of Single Silicon-Vacancy Spins in Diamond, *Phys. Rev. Lett.* **113**, 263602 (2014).
- [18] J. N. Becker, B. Pingault, D. Groß, M. Gündoğan, N. Kukharchyk, M. Markham, A. Edmonds, M. Atatüre, P. Bushev, and C. Becher, All-Optical Control of the Silicon-Vacancy Spin in Diamond at Millikelvin Temperatures, *Phys. Rev. Lett.* **120**, 053603 (2018).
- [19] L. J. Rogers, O. Wang, Y. Liu, L. Antoniuk, C. Osterkamp, V. A. Davydov, V. N. Agafonov, A. B. Filipovski, F. Jelezko, and A. Kubanek, Single Si - V - Centers in Low-Strain Nanodiamonds with Bulklike Spectral Properties and Nanomanipulation Capabilities, *Phys. Rev. Applied* **11**, 024073 (2019).
- [20] T. M. Hoang, J. Ahn, J. Bang, and T. Li, Electron spin control of optically levitated nanodiamonds in vacuum, *Nat Commun* **7**, 12250 (2016).
- [21] M. L. Juan, C. Bradac, B. Besga, M. Johnsson, G. Brennen, G. Molina-Terriza, and T. Volz, Cooperatively en-

- hanced dipole forces from artificial atoms in trapped nanodiamonds, *Nature Phys* **13**, 241 (2017).
- [22] A. C. Frangeskou, A. T. M. A. Rahman, L. Gines, S. Mandal, O. A. Williams, P. F. Barker, and G. W. Morley, Pure nanodiamonds for levitated optomechanics in vacuum, *New J. Phys.* **20**, 043016 (2018).
- [23] B. Pingault, D.-D. Jarasch, C. Hepp, L. Klintberg, J. N. Becker, M. Markham, C. Becher, and M. Atatüre, Coherent control of the silicon-vacancy spin in diamond, *Nat Commun* **8**, 15579 (2017).
- [24] K. G. Fehler, A. P. Ovyvan, L. Antoniuk, N. Lettner, N. Gruhler, V. A. Davydov, V. N. Agafonov, W. H. Pernice, and A. Kubanek, Purcell-enhanced emission from individual SiV<sup>-</sup> center in nanodiamonds coupled to a Si<sub>3</sub>N<sub>4</sub>-based, photonic crystal cavity, *Nanophotonics* **9**, 3655 (2020).
- [25] J. M. Binder, A. Stark, N. Tomek, J. Scheuer, F. Frank, K. D. Jahnke, C. Müller, S. Schmitt, M. H. Metsch, T. Unden, T. Gehring, A. Huck, U. L. Andersen, L. J. Rogers, and F. Jelezko, Qudi: A modular python suite for experiment control and data processing, *SoftwareX* **6**, 85 (2017).